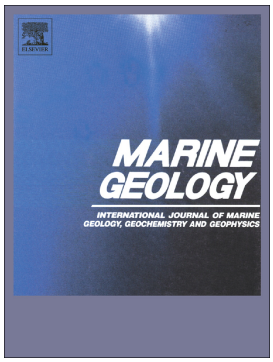

Bottom currents, submarine mass failures and halokinesis at the toe of the Sigsbee Escarpment (Gulf of Mexico): Contrasting regimes during lowstand and highstand conditions?

V. Maselli, B. Kneller

PII: S0025-3227(18)30045-8
DOI: doi:10.1016/j.margeo.2018.04.001
Reference: MARGO 5778

To appear in: *Marine Geology*

Received date: 6 February 2018
Revised date: 21 March 2018
Accepted date: 2 April 2018

Please cite this article as: V. Maselli, B. Kneller , Bottom currents, submarine mass failures and halokinesis at the toe of the Sigsbee Escarpment (Gulf of Mexico): Contrasting regimes during lowstand and highstand conditions?. The address for the corresponding author was captured as affiliation for all authors. Please check if appropriate. Margo(2017), doi:10.1016/j.margeo.2018.04.001

Title: Bottom currents, submarine mass failures and halokinesis at the toe of the Sigsbee Escarpment (Gulf of Mexico): contrasting regimes during lowstand and highstand conditions?

Authors

Maselli, V.[1], Kneller, B.[1]

[1]University of Aberdeen, Department of Geology and Petroleum Geology, Meston Building, King's College, Aberdeen, AB24 3UF, United Kingdom.

Highlights

1. Three types of mass transport complexes were recognised along the Sigsbee Escarpment.
2. Submarine mass failures were triggered by bottom currents and halokinesis.
3. Bottom currents were more energetic during interglacial intervals.
4. Halokinesis forced oversteepening of the Sigsbee Escarpment during glacial intervals.

Keywords

Mass transport complex, sediment drift, hazard, seismic geomorphology, Gulf of Mexico.

Abstract

In this study we explore the role of sediment supply, halokinesis and deep ocean circulation in promoting margin instability. The analysis was carried out on multibeam and high-resolution seismic data that allowed the imaging of mass failure deposits and current-driven depositional features along a portion of the lower continental slope and upper continental rise of the Sigsbee Escarpment (Gulf of Mexico). Different styles of deposition have been recognised during sea level lowstand (LST) and highstand (HST) conditions, due to alternating bottom current activity and salt tectonics. Lowstands are characterized by a reduced intensity of the Loop Current, as underlined by

the lack of current-driven erosional features. On the contrary, highstands show a strengthened Loop Current that generates a fast bottom current circulation, as suggested by the presence of extensive furrow fields on the modern sea floor and on the Marine Isotope Stage 5e palaeo-sea floor horizon. Increased sediment load combined with changes in the intensity of deep water circulation are also responsible for the instability of the Sigsbee Escarpment, triggering mass failure phenomena with distinct morphology, size, location and timing of emplacement. Type 1 mass transport complexes (MTCs) form on the upper continental rise during sea level fall, and are genetically linked to the growth of deep water sediment drifts. Type 2 MTCs develop during sea level lowstands and originate along the slope of the Sigsbee Escarpment, triggered by oversteepening generated by halokinesis. Type 3 MTCs form during sea level rise to highstand conditions and mostly consist of debris flow deposits, generated in the lower portions of the Sigsbee Escarpment and then accumulated in the upper continental rise.

1. Introduction

The transport and remobilization of coarse-grained sediment in deep water settings normally occur under the action of energetic events, such as turbidity currents, submarine landslides and subaqueous debris flows (Mutti and Normark, 1991; Hampton and Lee, 1996; Locat and Lee, 2005). Since the early 1950s (Heezen and Ewing, 1952), substantial efforts have been dedicated to the study of such processes, and to the understanding of their signature in the sedimentary record (Mulder and Syvitski, 1995; Kneller, 1995; Masson et al., 2006; Talling et al., 2007).

Mass-transport complexes (MTCs), which include slides, slumps and debris flows (Moscardelli and Wood, 2008), are a fundamental feature in the evolution of both active and passive continental margins, as they may account for up to 70% of the sediment accumulating in deep water settings (Moscardelli et al., 2006). MTCs have been widely investigated not only for their role in reshaping the sea floor morphology (Kneller et al., 2016, and references therein), but also for their relevance in the oil and gas exploration, as they may form key stratigraphic seals, especially when associated

with channel-levee complexes (Moscardelli et al., 2006; Alves et al., 2014), or they may generate confined slope accommodation, hosting ponded reservoirs (Kneller et al., 2016).

Submarine mass movements can occur as a long-term deformation without failure, as in the case of slow motion creeping (Mulder and Cochonat, 1996; Li et al., 2016), or as a sudden and catastrophic event, where huge amounts of sediment may be involved (Bryn et al., 2005a). Submarine mass failures can affect large portions of the continental margin, modifying the morphology of the sea floor and changing the pressure and temperature gradients of the buried sediments beneath. Consequently, MTCs may alter the oceanographic regime through shifting ocean bottom currents (Campbell and Deptuck, 2012), may reorganize sediment distribution pathways leading to the formation of local sediment depocenters (Alves and Cartwright, 2010; Kneller et al., 2016), and may impact global climate by triggering methane release from sub-sea floor sediment (Kennett et al., 2003; Maslin et al., 2004). In addition, modern mass failure events represent a hazard not only for infrastructure lying on, or directly connected to, the sea floor, but also for the surrounding costal zones that may be flooded by landslide-generated tsunamis (Nisbet and Piper, 1998; Casalbore et al., 2012; Tappin et al., 2014).

The evaluation of the risk associated with the failure of the sea floor in a specific setting requires a detailed understanding of the potential trigger mechanisms of margin instability. Several studies have investigated the processes that may be responsible for the initiation of submarine mass movements, including storm-wave loading, gas hydrate dissociation, oversteepening and rapid sediment accumulation (Henkel, 1970; Mienert et al., 1998; Kvenvolden, 1999; McAdoo et al., 2000; Cattaneo et al., 2003; Porębski and Steel, 2003; Harders et al., 2011; Zang et al., 2016).

The oscillatory motion associated with the passage of ocean waves can generate sediment failures on steep shelves characterized by soft and underconsolidated sediment, as along prodelta fronts or subaqueous clinoforms (Henkel, 1970; Cattaneo et al., 2003; Zang et al., 2016; Chiocci and Casalbore, 2017). More energetic and volumetrically larger submarine mass failures may occur due

to the dissociation of gas hydrates (Mienert et al., 1998; Kvenvolden, 1999) that can be originated by warming ocean bottom temperatures (Kennett et al., 2000), tectonic uplift (von Huene and Pecher, 1999), sea level fluctuations (Liu and Flemings, 2009), or rapid sediment accumulation (Dillon et al., 1998). Oversteepening of the sea floor may act as a potential trigger of submarine landslides, especially along convergent margins or in sedimentary basins affected by salt tectonics (Harders et al., 2011; McAdoo et al., 2000). Along passive continental margins, in contrast, high sedimentation rates can generate high pore pressure which can lead to sediment failure by reducing the critical shear stress (Wolinsky and Pratson, 2007). Rapid sediment accumulation characterizes the subaqueous delta fronts of prograding deltas in highstand (HST) conditions, while it may affect larger portions of the margin during lowstand (LST) conditions, when sea level fall forces delta migration towards the upper slope (Suter and Berryhill, 1985; Porębski and Steel, 2003; Gong et al., 2016; Pellegrini at al., 2017).

Beyond the shelf edge, in deep and ultra-deep water settings, sediment transport and remobilization are often controlled by the oceanographic regime. Energetic bottom currents not only promote sediment accumulation far from main sediment entry points but may also exert a paramount control on the whole architecture of the margin (Masson et al., 2002). Bottom currents have been widely explored in different settings (Hernández-Molina et al., 2008a and 2008b, Rebesco et al., 2014), through direct observations of the flow properties (Canals et al., 2006; Trincardi et al., 2007) or by analysing their legacy on the sea floor morphology (Stow et al., 2008). The internal stratigraphy of contourites and other current-driven rapidly-accumulated sediment drifts often shows mass failure deposits embedded within bottom current deposits (Martorelli et al., 2016; Miramontes et al., 2016; Pellegrini et al., 2016; Miramontes et al., 2018). Although the presence of internal weak layers acting as glide planes has been proposed to explain a potential preconditioning factor (Laberg et al., 2016), the processes leading to the excess in pore pressure within current-driven deposits and the role of bottom currents as a potential hazard for continental margin stability are still open issues

(Bryn et al., 2005b; Laberg and Camerlenghi, 2008). This picture is further complicated in salt-dominated slope settings, where frequent landslides generated by salt movements may obscure other potential trigger mechanisms.

In this study we focus on a portion of the lower continental slope and upper continental rise along the Sigsbee Escarpment (Gulf of Mexico, Figs. 1, 2) to explore the role of sediment supply, salt tectonics and bottom current activity in promoting margin instability. We aim to define the timing of when one process dominates over the others within a sequence stratigraphic framework, and to highlight the location and magnitude of sediment failure events in an attempt to link different types of MTCs to their trigger mechanism.

2. Gulf of Mexico: A brief overview

2.1. Basin History

The Gulf of Mexico is a semi-enclosed basin whose history started in the Late Triassic during the breakup of Pangea (Martin, 1978). Dominant sediment deposition changed through time, reflecting the evolution of the basin and the formation of North American orogens. Several kilometres thick salt deposits (the Louann Salt) accumulated during the late Middle Jurassic, followed by carbonate deposition until the Late Cretaceous (Martin and Bouma, 1978). Clastic sediment started to accumulate in the northern Gulf of Mexico during the Paleocene (Coleman et al., 1986), reaching a total thickness of up to 15 kilometres during the Cenozoic (Martin and Bouma, 1978), partially as a consequence of the formation of the Mississippi River drainage basin (Blum and Pecha, 2014).

2.2. Sea floor Morphology

The north-eastern margin of the Gulf of Mexico comprises the carbonate platform of the Florida Terrace and the Florida Escarpment (Fig. 1). The northern edge of this escarpment is occupied by the De Soto Canyon (Fig. 1). Farther to the west, the U-shaped Mississippi Canyon dissects the slope and feeds the Mississippi Fan, a large deep sea fan system formed during the Plio-Pleistocene

(Moore et al., 1978; Fildani et al., 2017). The Mississippi Canyon is bounded to the west by the Texas-Louisiana (TX-LA) Slope, a large area dissected by domes and basins generated by salt tectonics (Diegel et al., 1995). Basinward, the lower continental slope terminates in the Sigsbee Escarpment (Buffler, 1983), a continuous morphological step locally interrupted by canyons. The escarpment shows more than 700 m of relief with slopes greater than 20° (Fig. 2) and represents the composite leading edge of a canopy of allochthonous Louann salt. The Rio Grande Slope separates the TX-LA Slope from the East Mexican Slope in the north-western portion of the Gulf of Mexico (Fig. 1).

2.3. Oceanographic setting

The surficial oceanographic regime of the Gulf of Mexico is dominated by the Loop Current, a warm, clockwise circulation that enters the basin through the Yucatan Channel and then flows back into the North Atlantic Ocean through the Strait of Florida (Fig 1; Nowlin, 1972). The flow path of the Loop Current may remain confined to the south-eastern Gulf of Mexico, or may extend to the north until reaching the TX-LA Slope (Huh et al., 1981). Clockwise-rotating eddies separate aperiodically from the Loop Current (Sturges et al., 1993) with surface speeds of more than 2 m s^{-1} (Cooper et al., 1990). In addition to the Loop Current and associated eddies, two significant long-period circulation gyres (cyclonic and anticyclonic) are generated by the action of the wind. Energetic deep water currents, anti-clockwise (Fig. 1), have been observed in the Gulf of Mexico. They range from barotropic topographic Rossby waves, generated by the combined effect of Loop Current and separated eddies (Hamilton, 1990; Hamilton 2009), to currents resulting from episodic atmospheric events, such as hurricanes (Nowlin et al., 1998). Direct observations of the velocity of deep water currents in the study area (Niedoroda et al., 2003a) have been obtained through the deployment of a current meter located at the base of the Sigsbee Escarpment, 10 m above the sea floor (Niedoroda et al., 2003a). The mean flow velocity from a 1.5 yr long record was ca. 25 cm s^{-1} while the fastest speed reached 126 cm s^{-1} (Niedoroda et al., 2003a).

3. Study area

The present study focuses on a portion of the lower continental slope and upper continental rise along the Sigsbee Escarpment in the area of the Atlantis oil field, in water depths between 1370 m and 2100 m (Figs. 1, 2). Since the discovery of the Atlantis field, several studies have been dedicated to the understanding of geotechnical properties, pore pressure regime and sedimentation history of this portion of the Sigsbee Escarpment, in order to evaluate the stability of the slope and to quantify the recurrence time of potential hazardous events, such as landslides, debris flows and turbidity currents (Al-Khafaji et al., 2003; Nadim et al., 2003; Niedoroda et al., 2003a and b; Nowacki et al., 2003; Orange et al., 2003a and b; Slowey et al., 2003; Young et al., 2003; Prieto et al., 2014; Prieto et al., 2016). The development of the escarpment has reflected the dynamic evolution of the salt under the effect of cyclic loading due to sedimentation and eustasy (Swierz, 1992). In places the salt crops out at the sea floor. The rugged topography of the escarpment has been formed by a combination of processes (salt tectonics, dissolution, bottom currents, sedimentation) that favored the development of submarine landslides (Peel et al., 1995; Nibbelink, 1999) in both the lower continental slope and the upper continental rise (Fig. 2). Al-Khafaji et al. (2003), Slowey et al. (2003) and Young et al. (2003) provide a detailed analysis of sea floor and sub-sea floor sediment characteristics based on a combination of box-cores, piston cores and deep soil boreholes. Their results show that the region consists of pelagic and hemipelagic sediments, predominantly made of high plasticity clays (Al-Khafaji et al., 2003), interbedded with mass failure deposits (Niedoroda et al., 2003a and b; Orange et al., 2003a).

4. Data and methods

The study area was investigated using a combination of AUV multibeam bathymetry and three-dimensional high-resolution (3D-HR) seismic data, taking also into account the information available from the literature. Multibeam bathymetry data were collected by BP Exploration &

Production Inc. for the Atlantis geohazard site survey by using a 200-kHz Simrad EM-2000 swath bathymetric system mounted on the Hugin 3000 AUV (Lee and George, 2004). Acquisition lines were oriented NNW-SSE, as highlighted by the acquisition artefacts visible in Figure 3. Multibeam data were gridded at 1.8 × 1.8 metre of horizontal resolution.

The seismic dataset, depth-migrated, has a peak frequency of about 175 Hz and covers 1200 km^2 (Fig. 3). Based on acoustic facies and reflection geometries, eight seismo-stratigraphic units (U-1 to U-8) confined by eight seismic horizons (H0 to H7) plus the sea floor were identified and mapped in the upper continental rise (Figs. 4, 5, 6). Each unit and bounding surfaces were characterized using a combination of 2D arbitrary lines extracted from the 3D seismic volume, seismic attributes, structural and thickness maps (each at 25 × 25 metres of horizontal resolution). Seismic attributes include both time-derived (variance) and amplitude-derived (root-mean-square, RMS) values. Variance, which is the equivalent of coherence or semblance, measures the similarity of consecutive waveforms over a given sampling window (3 × 3 traces in the present study), and it is useful for imaging lateral discontinuities, such as faults or channel margins (Chen and Sidney, 1997; Brown, 2011). RMS amplitude represents the square root of the arithmetic mean of the squares of the amplitudes within a defined window interval (6 instantaneous traces in the present study), and it is helpful for revealing bright spots, coarse-grained facies and unconformities (Rijks and Jauffredlk, 1991; Chen and Sidney, 1997; Brown, 2011).

5. Results

5.1a. Unit U-1

Unit U-1 (Fig. 7) is the deepest unit investigated in this study; it is bounded by horizon H0 at its base and horizon H1 at its top (Figs. 4, 6).

Horizon H0 is characterized by a continuous and high-amplitude positive reflection that maintains the same seismic character through the entire study area (Figs. 4, 5a, 6).

The surface map of horizon H0 (Fig. 7a) shows, from west to east:

1- A topographic depression about 25 m deep, labelled α (Figs. 7 a, e), which is about 30.5 km^2, is located in the NW corner of the study area and is flanked on its eastern side by a N-S trending ridge.

2- A triangular-shaped topographic depression, labelled β (Figs. 7 a, e), which is about 72 km^2 and is located in the central part of the study area. β enlarges and deepens towards SSE reaching a maximum depth of ca. 65 m compared to its shoulders, it is flanked by a N-S trending ridge on its western side (Figs. 7a, e), while its eastern side is characterized by a scalloped margin (Figs. 7a, e).

3- A flat area gently dipping toward SE and characterized by irregularly shaped topographic highs (Fig. 7a).

The RMS amplitude map (Fig. 7b) shows high values along the southern part of the scalloped margin and in the NE corner of the study area. Moreover, a series of NNW-SSE oriented lineaments with low RMS amplitude values can be identified along the ridge and eastward of the scalloped margin (Fig. 7b) and probably reflect seismic acquisition artefacts. The variance map (Fig. 7c) highlights the scalloped margin on the eastern side of β and the topographic highs in the eastern side of the study area. Horizon H0 across topographic lows α and β shows an erosional character, as highlighted by its irregular morphology and by the large lateral changes in the variance attribute (Figs. 7a, c).

On seismic sections, unit U-1 was divided into lower and upper sub-units (Figs. 4, 5b, 6). The lower sub-unit consists of highly discontinuous and high-frequency reflections, laterally changing from low to high amplitude (Fig. 5b), while the upper sub-unit is characterized by a strong reflection with negative polarity and high lateral continuity with little amplitude variation (Fig. 5b). Unit U-1, up to 25 metres thick, preferentially accumulates on the eastern side of the ridge (SD-1, Fig. 7d); as a consequence, Unit U-1 fills depression β asymmetrically, with a sigmoidal shape clearly visible in Figures 4 (seismic line 2) and 7e (section CD). Another small depocenter forms between the topographic highs on the eastern side of the study area (Fig. 7d).

5.1b. Interpretation

The erosional character of H0 across topographic lows α and β, which are bounded by a ridge and a scalloped margin with high RMS amplitude values, and the presence of irregularly shaped topographic highs, suggest that horizon H0 formed as a consequence of a major erosional event, probably generated by a submarine landslide. The lateral changes in the seismic variance not only reflect the rough topography of the horizon but may also highlight that the basal erosion exposed a dipping layered substrate (Fig. 7c). In the lack of direct sources of sediment in the proximity of the study area, such as submarine canyons and turbidite channels, the lateral thickness change of Unit U-1 and the formation of an asymmetric depocenter (SD-1, Fig. 7d) may suggest that U-1 accumulated under the action of bottom currents, flowing westward and forcing deposition against the ridge and the topographic highs.

5.2a. Unit U-2

Unit U-2 (Fig. 8) lies between horizons H1 and H2 (Figs. 4, 6).

Horizon H1 is characterized by a continuous, positive and high-amplitude reflection that shows a constant seismic character in much of the study area (Figs. 4, 6).

The surface map of horizon H1 (Fig. 8a) resembles the general morphology of horizon H0, with the presence of both depressions α and β (Figs. 8a, e), the N-S trending ridge and the topographic highs farther to the east. A diagnostic character of the horizon is the presence of longitudinal features (Fig. 8a), oriented SW-NE to WSW-ENE and showing a width of 20-75 metres, a depth of 1-4 metres, a spacing of 30-120 metres, and a length up to several kilometres.

The RMS amplitude map (Fig. 8b) shows low values along the ridge, with little variations associated to the longitudinal features observed in the surface map, suggesting the presence of homogeneous sediment. High RMS amplitude values are visible on the eastern portion of the study

area (Fig. 8b). The variance map (Fig. 8c) better highlights the longitudinal features observed in the surface map (Fig. 8a).

On seismic sections, such features appear as v-shaped small-scale incisions (Figs. 4, 5c). Unit U-2 can be divided into two sub-units (Fig. 5d): a lower sub-unit consisting of continuous and high amplitude reflections (Fig. 5d) slightly converging toward SSE (Fig. 4) to E (Fig. 6), and an upper sub-unit characterised by discontinuous to semi-transparent seismic facies (Fig. 5d). Unit U-2 shows higher sediment accumulation within the topographic low β (SD-1, Fig. 8d), mostly focused on the eastern side of the ridge with a sediment thickness up to 32 m, and towards the northern part of the study area, with a sediment thickness up to 45 m (SD-2, Fig. 8d). In some areas Unit U-2 is missing, as highlighted in seismic lines 1 (Fig. 4) and 4 (Fig. 6). Areas of no deposition or erosion are characterised by RMS positive anomalies (Fig. 8c).

5.2b. Interpretation

Elongated erosional features similar to the lineaments visible on horizon H1 have been identified in other margin settings, such as the Blake-Bahama Outer Ridge (Flood, 1983) and the Gulf of Lyon (Puig et al., 2008), and have been described as sedimentary furrows (Flood, 1983). Furrows are longitudinal features that form in areas of strong or persistent bottom currents over cohesive sediment, and may develop when deposition exceeds erosion or vice versa (Flood, 1983). Based on their morphology and spatial distribution, the furrows on horizon H1 resemble the type 1C furrows defined in Flood (1983). The presence of type 1C furrows on horizon H1 suggests that erosion exceeded deposition at the time of the formation of horizon H1 and that bottom current velocity increased after deposition of Unit-1. The accumulation of unit U-2 above the furrowed surface and the asymmetric geometry of SD-1 (Fig. 8d) indicate that this interval recorded a progressive change from strong to weaker bottom currents.

5.3a. Unit U-3

Unit U-3 (Fig. 9) lies between horizons H2 and H3 (Figs. 4, 6).

Horizon H2 is characterized by a continuous positive reflection, laterally changing from low to high-amplitude (Figs. 4, 5e), and can be traced across much of the study area.

The surface map of horizon H2 (Fig. 9a) still presents topographic depressions α and β, now showing a narrower morphology due to the deposition of Unit U-2. The furrow fields visible on horizon H1 are now draped and less evident (Fig. 9a). The ridge presents a mounded morphology (Fig. 9a, e), with a steeper western flank characterised by an irregular topography (section AB in Fig. 9e), as the eastern side of β (section CD in Fig. 9e).

The RMS amplitude map (Fig. 9b) shows low values along the ridge and high values where the topography of the horizon H2 is irregular (Fig. 9a). The variance map (Fig. 9c) better highlights the draped furrows observed in the surface map (Fig. 9a).

On seismic sections, Unit U-3 is characterized by high-frequency continuous to discontinuous reflections, mostly low amplitude and locally converging (Figs. 4, 5f, 6d). Unit U-3 shows higher sediment accumulation on the eastern side of the N-S trending ridge, where SD-1 is up to 32 m thick (SD-1, Fig. 9d) and toward the northern part of the study area, where SD-2 is up to 37 m thick (Fig. 9d). The thickness of SD-1 decreases laterally eastward (Fig. 9d), where non-deposition/erosion occurs on the eastern flank of the topographic depressions β (see section CD in Figure 9e). Here, the RMS amplitude map shows the highest variability, with large positive anomalies (Fig. 9c). In some places, where the thickness of the underlying Unit U-2 approaches zero, H2 is associated with an erosional surface where more than one horizon coincides (Figs. 4, 6).

5.3b. Interpretation

The irregular topography of horizon H2 and the lateral thickness changes of Unit U-3 can be ascribed to a combination of post-depositional erosion of the unit, as highlighted by the reflection terminations (Figs. 4, 6), and lateral thinning associated with asymmetric deposition, as suggested by the convergence of the seismic reflections (Fig. 6, seismic line 3). This evidence suggests that

bottom currents were active at the time of deposition, as testified by the asymmetric geometry of SD-1 and SD-2, although less energetic, due to the lack of furrows.

5.4a. Unit U-4

Unit U-4 (Fig. 10) lies between horizons H3 and H4 (Figs. 4, 6).

Horizon H3 is characterized by a continuous positive reflection, changing laterally from low amplitude in the northern part of the study area to high amplitude in the southern part (Figs. 4, 5g, 6). The horizon can be traced across the study area, although, when Unit U-3 is missing (Fig. 9e), it corresponds to an erosional surface.

The surface map of horizon H3 (Fig. 10a) is still characterised by topographic depressions α and β, and shows an irregular topography on the western flank of the ridge and on the eastern side of β (Fig. 10a). Due to the asymmetric deposition of units U-1 to U-3 on the western side of β, the N-S trending ridge now presents a mounded morphology that resembles the geometry of a sediment drift (Fig. 10a). On the eastern side of this sediment drift, the surface map highlights the presence of an escarpment, up to 15-17 metres in elevation and running almost W-E (Fig. 10a).

The RMS amplitude map (Fig. 10b) shows low values along the sediment drift and high values where horizon H3 is characterized by an irregular topography (Fig. 10a). The escarpment, visible on both the RMS amplitude (Fig. 10b) and the variance maps (Fig. 10c), is highlighted on a 2D arbitrary seismic line by a series of truncated reflections (Fig. 11, seismic line 5).

On seismic sections, unit U-4 is marked by discontinuous to chaotic reflections (Figs. 4, 5h, 6). The thickness of U-4 changes across the study area, and an area of reduced sediment thickness can be observed on the western side of the sediment drift (Fig. 10d), where horizon H3 is characterized by high RMS amplitude values (Fig. 10b). A sediment depocenter (SD-3, morphometry provided in Table 1) develops at the southern limit of the study area and partially fills the topographic low along its axis (Fig. 10d). SD-3 consists of high amplitude and continuous reflections, locally wavy and interbedded with a more chaotic facies (Fig. 11). A series of consecutive time slices extracted at 10

m interval from the variance attribute seismic cube shows sub-circular features, lying above horizon H3, that correspond to higher amplitude reflections on a 2D seismic section (Fig. 11).

5.4b. Interpretation

The geometry and location, confined in a topographic low downslope of an escarpment, its seismic facies and internal architecture, support the interpretation that sediment depocenter SD-3 is the result of a submarine mass failure event (whose outline is highlighted in light blue in Figs. 10e and 11). This interpretation is further supported by the presence of truncated reflections where the head scarp is located and of landslide blocks downslope from the escarpment (Fig. 11).

5.5a. Unit U-5

Unit U-5 (Fig. 12) lies between horizons H4 and H5 (Figs. 4, 6).

Horizon H4 is characterized by a positive reflection, laterally changing from continuous to discontinuous and from low amplitude to high amplitude (Figs. 4, 5i, 6). Horizon H4 can be traced across the study area, although in some places it merges with the shallower horizon H5 due to the highly erosional character of the latter (seismic line 2 in Figure 4, and seismic line 4 in Figure 6).

The surface map of horizon H4 (Fig. 12a) shows the N-S trending sediment drift flanked by topographic depressions α and β. The southern part of β is now characterized by a flat surface lying at ca. -2450 m (Fig. 12e) and generated by the emplacement of SD-3 along the axis of β. North of this area, an arcuate escarpment about 10 metres high can be detected (Fig. 12a); it is also visible in both RMS and variance maps (Figs. 12b, c).

The RMS amplitude map (Fig. 12b) presents low values along the sediment drift and high values both on its western and eastern sides. Moreover, the eastern side shows an alternation of high-low-high RMS amplitude, oriented N-S and associated respectively with lower-higher-lower surface elevations (Fig. 12b).

The distribution of Unit U-5 resembles a lens-shaped geometry in cross-section (Figs. 4, 6), with a constant sediment thickness along the N-S direction but with lateral (W-E) thickness changes from 40 m to ca. 0 m (Fig. 12d). The areas with reduced sediment thickness (light grey in Fig. 12d) also correspond to high RMS amplitude values (Fig. 12b). A sediment depocenter (SD-4, morphometry provided in Table 1) up to 58 metres thick and oriented WNW-ESE formed in the central part of the study area (Fig. 12d). This body accumulated along the axis of the topographic depression β, without reaching its southern limit (Fig. 12d) due to the confinement generated by SD-3 (Fig. 10d). On seismic sections, Unit U-5 is characterized by three seismic facies (Figs. 4, 5j, k, l): the first one, detected primarily where the RMS amplitude is low on the mounded drift, shows discontinuous low amplitude to transparent reflections (Fig. 5j); the second one, detected toward the southern limit of the study area along the axis of the topographic depression β, presents parallel and continuous high amplitude reflections (Figs. 6k, 13); the third one, that is associated with the sediment depocenter SD-4, shows continuous to discontinuous high amplitude reflections, parallel to wavy, and locally alternating with a more transparent or chaotic seismic facies (Figs. 6l, 13). A closer look at the seismic data highlights that the sediment depocenter SD-4 can be divided into 2 sub-units (SD-4 lower and SD-4 upper, Figs. 12e, 13), characterized by similar seismic facies but separated by a continuous negative reflection (the yellow dashed lines in Figure 13). The areal extent can be fully quantified for SD-4 lower (green area in Figure 12e, Table 1), but not for SD-4 upper (orange area in Figure 12e, Table 1). Moreover, the toe of the SD-4 lower can be detected on both RMS amplitude and variance maps (Figs. 12b, c, 13).

5.5b. Interpretation

A combination of morphological evidences and seismic data support the hypothesis that sediment depocenter SD-4 formed by a combination of two mass failure events, named SD-4 lower (green in Figs. 12e, 13) and SD-4 upper (orange in Figs. 12e, 13). The headwall scarp of SD-4 lower landslide can be traced along the escarpment detected on the surface map of horizon H4 (Fig. 12a),

while the source area of SD-4 upper has been probably eroded during the emplacement of unit U-6 (see next section), as also suggested by the reduced sediment thickness of U-5 in this area (Fig. 12d) and by the high RMS amplitude values associated to the erosional character of horizon H4 (Figs, 4, 6, 12b).

5.6a. Unit U-6

Unit U-6 (Fig. 14) lies between horizons H5 and H6 (Figs. 4, 6).

Horizon H5 is characterized by a high amplitude reflection couplet that locally appears wavy to irregular (Figs. 4, 5m, 6).

The surface map of horizon H5 (Fig. 14a) has a complex topography within the study area, changing laterally from W to E (Fig. 14a). The western part is characterized by topographic depression α and by the N-S trending sediment drift (Fig. 14b). Farther to the east, where β occurs, the surface map shows a very rough topography marked by linear and arcuate incisions, mostly N-S trending (Fig. 14a). In the northern part, the study area reveals two elongated topographic depressions that widen and deepen southward (i.e. downslope). Moreover, in the south-eastern corner of the study area (Fig. 14a), the surface map presents a box-shaped depression (indicated by a red arrow in Figure 14a), dipping toward WSW and bordered by two escarpments oriented WSW-ENE.

The RMS amplitude map (Fig. 14b) shows low values along the crest of the sediment drift and farther to the west, while high and variable values, often organized in N-S trending lineaments, characterize the area with a rough topography (Fig. 14a). The elevated palaeo-sea floor between the two lows recognised in the northern part displays high RMS amplitude values (Fig. 14b).

The variance map (Fig. 14c) better highlights the linear and arcuate incisions where β occurs, and the two escarpments oriented WSW-ENE (Fig. 14a, c).

On seismic sections (Figure 4, seismic line 2, and Figure 15), the linear and arcuate incisions visible on the surface map (Fig. 14a) appear as box-shaped, few metres deep and bounded by steep flanks.

Unit U-6 predominantly occupies the area associated with the rough topography highlighted on the surface map (Fig. 14a, d), showing a greater thickness downslope (Fig. 14d). The entire unit can be seen as a major sediment depocenter (SD-5, morphometry provided in Table 1) reaching a maximum thickness of ca. 80 metres (Fig. 14d). A second small depocenter (SD-6, ca. 25 metres thick) is associated with the box-shaped depression identified on the eastern part of the study area (Figs. 14a, d). Westward, Unit U-6 is almost draping the pre-existing sea floor topography with an average thickness of about 10 metres (Fig. 14d).

In seismic profiles, sediment depocenters SD-5 and SD-6 present a chaotic seismic facies, locally showing discontinuous low amplitude reflections (Figs. 4, 5n, 15).

5.6b. Interpretation

The morphology of horizon H5 and the seismic facies of sediment depocenter SD-5 (Figs. 14, 15) suggest that this unit is the consequence of a major mass failure event, probably originated along the Sigsbee Escarpment outside the study area. The energetic downslope movement of the landslide body eroded the palaeo-sea floor creating the linear incisions that characterize surface H5; such features are described in the literature as basal striations or grooves (e.g. Gee et al., 2005). The downslope erosion associated with the emplacement of SD-5 probably generated a second mass failure (SD-6) through basal incision, as suggested by the direction of movement of the latter toward WSW (Fig. 14d).

5.7a. Unit U-7

Unit U-7 (Fig. 16) lies between horizons H6 and H7 (Figs. 4, 6).

Horizon H6 is characterized by a low amplitude positive reflection when it forms on top of the mounded sediment drift (Figs. 4, 5o), while presenting a high amplitude reflection, locally wavy, when it lies on top of the landslide SD-5 (Figs. 4, 5o).

In the surface map of horizon H6 (Fig. 16a) the N-S trending sediment drift is still a prominent feature of the palaeo-sea floor, although it was partially covered by the MTC on its eastern flank (Fig. 16a). On top of the landslide, horizon H6 shows both a flat to convex-up, slightly irregular topography (section CD in Fig. 16e), and the presence of landslide blocks in its north-eastern corner (Fig. 16a).

The RMS amplitude map (Fig. 16b) displays low values across the eastern side of the sediment drift and the top of the landslide SD-5, while high values characterise the NW flank of the drift (Fig. 16b). The variance map (Fig. 16c) highlights the irregular topography of horizon H6, the landslide blocks on north-eastern corner of the study area (Figs. 16a, c), and also a small furrow field in its north-western corner (Fig. 16c).

On seismic sections, Unit U-7 is dominated by discontinuous low amplitude reflections (Figs. 4, 5p, 6) that form a slightly sigmoidal unit (Fig. 5, seismic line 3). Unit U-7 covers much of the horizon H6 with an average thickness of ca. 10 metres (Fig. 16d); sediment thickness is lower in the area characterized by high RMS values (Figs. 16a, d). Slightly asymmetric deposition and the development of a small sediment depocenter (SD-7) can be seen on the eastern flank of the sediment drift (Fig. 16d).

5.7b. Interpretation

Horizon H6 developed after the emplacement of the large mass failures associated with sediment depocenters SD-5 and SD-6, and the deposition of Unit U-7 occurred during a period of reduced bottom current activity, as suggested by its slightly asymmetric geometry (Figs 16d, e). The high RMS values that characterise H6 in the western part of the study area (Fig. 16b) are probably artefacts generated because of the sampling window applied for calculating the seismic attribute: due to the reduced thickness of unit U-6 in this area, the calculation of the RMS may have included the high values of the horizon H7 at the top of the unit. The same artefact may explain the presence

of a small furrow field visible in the north-western corner of the variance map (Fig. 16c) but not of the surface map of horizon H6 (Fig. 16a).

5.8a. Unit U-8

Unit U-8 (Fig. 17) lies between horizon H7 at its base and the sea floor (Figs. 4, 6).

Horizon H7 is marked by a continuous high amplitude reflection toward the northern part of the study area (Figs. 4, 5q) while showing a discontinuous low amplitude character downslope, in deeper water (Figs. 4, 5q).

The surface map of horizon H7 (Fig. 17a) presents the N-S trending sediment drift, now wider on its norther part, and a flat to slightly convex-up area toward the east. Another small sediment drift can be detected on the NW corner of the study area (Fig. 17a).

The RMS amplitude map (Fig. 17 b) shows low values on the eastern side of the sediment drift and farther eastward, while a large area of high RMS amplitude values characterises the western side of the mounded sediment ridge, almost matching the position where Unit U-8 is lacking or extremely reduced in thickness (Fig. 17d).

The variance map (Fig. 17c) reveals the presence of longitudinal features, oriented between SW-NE and WSW-ENE, in the area bordering the top of the mass failure SD-5 of Unit U-6 (Fig. 16d).

On seismic sections, unit U-8 is characterized by high-frequency and low amplitude reflections (Fig. 5r), laterally changing from continuous to discontinuous, locally converging (Figs. 4, 6). Unit U-8 displays an asymmetric thickness across the N-S trending sediment drift, with a large area of reduced sediment accumulation along its western flank and a sediment depocenter (SD-7) on its eastern flank (Fig. 17d). Two new triangular-shaped depocenters (SD-8 and SD-9, Fig. 17d) can be detected on the north-eastern corner of the study area. The internal stratigraphy of SD-8 and SD-9 (visible in line 4 of Figure 6) is characterised by a chaotic seismic facies made up of discontinuous and high amplitude reflections (Fig. 5s). SD-8 and SD-9 are visible on the modern sea floor, as highlighted in Figure 18a and on the AUV bathymetry of Figure 19.

5.8b. Interpretation

Based on seismic facies and internal geometry, sediment depocenters SD-8 and SD-9 may represent two debris flows deposits that originated in the lower part of the Sigsbee Escarpment. This interpretation is in agreement with the results presented by Young et al. (2003) and Niedoroda et al. (2003a), who also dated the deposits at around 10 kyr BP. The longitudinal features visible on the variance map (Fig. 17c) can be interpreted as sedimentary furrows, as for the lineaments visible on horizon H1 (Fig. 8c). Those features are noticeable mainly in the variance map (Fig. 17c) rather than in the surface map of horizon H7 (Fig. 17a), probably as a consequence of the sampling window used for calculating the seismic attribute: due to the reduced thickness of unit U-7 in this area, the window may have included reflections just above the horizon, where the furrows are instead present (see Fig. 18a). This means that fast bottom currents able to erode the sea floor started at some point during the accumulation of Unit U-8, and not at the time of horizon H7 deposition that was anyhow affected by low-energy bottom currents, as suggested by the asymmetric thickness of SD-7 within unit U-8 (Fig. 17d).

5.9a. Sea floor horizon

The sea floor horizon has been extracted from the 3D seismic data (Fig. 18a) and compared with the higher resolution AUV multibeam bathymetric data (Figs. 3, 19). On seismic sections, the sea floor horizon appears as a continuous high amplitude reflection couplet, characterized by small-scale undulations (Figs. 4, 5t).

In map view, the modern sea floor (Fig. 18a) reveals the N-S trending sediment drift, the small sediment drift on its western side and a new drift on its eastern side, which is confined by debris flow SD-8 and SD-9 (Fig. 18a). The debris flow deposits appear as elongated relieves with a rough morphology (Figs. 18a, 19). The most prominent feature characterizing the sea floor is the presence of extensive furrow fields (Figs. 18a, 19). The furrows show a width of 2-15 metres, a spacing of 2-

20 metres, and a depth of 0.5-3 metres, with the deeper scours occurring on top of the sediment drifts. Furrow fields develop in much of the study area, with the exception of the topographic lows in between the sediment drifts and on top of SD-8 and SD-9 (Fig. 19).

The RMS amplitude map (Fig. 18b) presents a series of NNW-SSE oriented lineaments with alternating low-high values that probably reflect seismic acquisition artefacts, and two triangular-shaped areas with high amplitude that correspond to SD-8 and SD-9 (Fig. 18b).

The variance map (Fig. 18c) highlights the furrow fields and the steep western flank of the N-S trending sediment drift.

5.9b. Interpretation

The presence of a series of mounded sediment drifts and furrow fields suggests that deposition occurred under the action of energetic bottom currents that, at times, were fast enough to partially rework sea floor sediments. The lack of furrows on top of SD-8 and SD-9 suggests that the upper surfaces of these debris flows were resistant to erosion by the bottom currents. This interpretation is in agreement with Prieto (2016), who presented a detailed investigation of the furrow fields based on high-resolution chirp seismic profiles and side-scan sonar data.

5.10. Chronological framework

Slowey et al. (2003) and Young et al. (2003) used radiocarbon dating and nannofossil biostratigraphy from boreholes ASB-3 and ASB-4 (see location in Figure 3) to constrain the chronology of the upper 150 metres of the sedimentary succession. Beyond the domain of radiocarbon dating, coccolithophore assemblages provided a robust framework for the chronology of the Late Quaternary, with the last occurrence of *Pseudoemiliania lacunosa* dated at ca. 500 kyr BP, the first occurrence of *Emiliania huxleyi* at 290 kyr BP and its initial dominance dated at ca. 75 kyr BP (Slowey et al., 2003). Seismic tie to the boreholes constrained the ages of horizon H0 and H5 to 75-290 kyr BP and to 45,740-21,140 yr BP, respectively (Figs. 20, 21c). The chronology of

horizon H7 (Fig. 21d), furthermore, is supported by the fact that a series of debris flow deposits occurs just above the horizon in the northern part of the study area and are dated to ca. 10 kyr BP (Niedoroda et al., 2003a). Additional chronological constraints may be derived indirectly considering the similarity between the modern sea floor and horizon H1, both characterized by extensive furrow fields with analogous orientation (Figs. 8, 18). It is therefore possible that horizon H1 may have developed during oceanographic conditions similar to those observed today, and thus during the last interglacial sea level highstand of Marine Isotopic Stage (MIS) 5e, at ca. 125 kyr BP (Figs. 21a, b, e, f). As a consequence, horizon H0 might be as old as MIS 6 sea level lowstand (Fig. 21f). Combining the information presented above, we propose a model for the chronology of the eight seismic horizons, where colour bars represent age uncertainties (Fig. 21f).

5.11. MTCs classification

The mass transport complexes identified in this study were grouped into three different types based on their morphology, size and location (Table 1).

Type 1 MTCs are associated with sediment depocenters SD-3, SD-4 lower and SD-4 upper. These MTCs accumulated in the upper continental rise on the eastern side of the N-S trending sediment drift (Figs. 10, 12), and present, on average, similar run-out distances, volumes and areal extents (Table 1). Based on their morphometry, type 1 MTCs can be classified as detached MTCs using the definition of Moscardelli and Wood (2008). When visible, the head scarp and the toe of the landslides show arcuate geometries (Figs. 10a, 12a), while the basal surface is almost planar, probably indicating a translational mechanism of emplacement (Hampton et al., 1996).

Type 2 MTCs are represented by the mass failure deposit associated with the large erosional surface of horizon H0 (Fig. 7a) and by the sediment depocenter SD-5 (Fig. 14). SD-5 has a run-out distance of at least 16 km, as the head scarp is difficult to identify precisely on the 3D seismic data while the toe is outside the dataset. Based on their morphometry, type 2 MTCs can be classified as attached MTCs using the definition of Moscardelli and Wood (2008).

Type 3 MTCs are associated with the sediment depocenters SD-8 and SD-9 (Fig. 17d); both MTCs lie on horizon H7 and are visible on the modern sea floor (Figs. 18, 19). Type 3 MTCs accumulated at the base of the Sigsbee Escarpment, remaining confined in the troughs of the sediment drifts (Figs. 18, 19), and are characterized by small volumes, areas and run-out distances if compared with type 1 and type 2 MTCs. Using the definition of Moscardelli and Wood (2008), type 3 MTCs can be classified as detached MTCs.

6. Discussion

6.1. Bottom current activity

Among palaeoceanographic studies, the quantification of palaeocurrent activity has been considered of paramount importance (Bianchi and McCave, 1999). When sub-sea floor sediment samples are available, changes in bottom current velocity can be derived from the sediment grain size distribution, quantifying in particular the mean sortable silt fraction (i.e., 10 to 63 μm) that is considered as a robust current strength indicator (McCave et al., 1995). In the absence of direct sediment sampling, variations in bottom current velocity can be inferred looking at the vertical and spatial changes of the sediment architecture on acoustic data (Faugères et al., 1999; Hernández-Molina et al., 2006), or identifying bottom current indicators on sea floor and palaeo-sea floor surfaces (Masson et al., 2004; Dunlap et al., 2013). In this study, temporal variations in the intensity of bottom currents in the upper continental rise of the Gulf of Mexico have been obtained using a combination of seismic horizon maps (considered as palaeo-sea floor surfaces), thickness maps and 2D arbitrary seismic sections. The modern sea floor (Figs. 18a, 19) is a snapshot of the continuous evolution of the margin under the action of fast bottom currents, as testified by the presence of extensive furrow fields (Fig. 18). This observation is supported by direct measurements of bottom current flow velocity that in the study area reaches more than 100 cm s^{-1} (Niedoroda et al., 2003a). Fast bottom currents were active during the deposition of unit U-8, not at horizon H7, as testified by the presence of furrow fields only on the variance map of H7 (Fig. 17c). The available

geochronological data in the area (Young et al., 2003; Niedoroda et al., 2003a, Figs. 20, 21) constrain the age of horizon H7 to the Holocene and consequently link the onset of an energetic bottom current regime to highstand sea level conditions. This hypothesis is further supported by the palaeoceanographic reconstruction of the Loop Current, considered the driver of the deep water circulation in the Gulf of Mexico (Shanmugam, 2006; Hamilton, 2009), showing strengthened flows during interglacial conditions due to the northward shift of the Intertropical Convergence Zone (Poore et al., 2003; Nürnberg et al., 2008). Sediment accumulation under the action of bottom currents, although less energetic, probably occurred during the entire interval investigated in this study, as testified by the presence of asymmetric sediment depocenters accumulating through time, especially during deposition of units U-7 (Fig. 16), U-3 (Fig. 9), U-2 (Fig. 8). By contrast, units U-6 (Fig. 14), U-5 (Fig. 12) and U-4 (Fig. 10) were affected by mass wasting processes that disrupted the original stratification and sediment distribution thickness (Figs. 10, 12, 14). Correlation with soil borings ASB-3 and ASB-4 (Figs. 20, 21) highlights that unit U-6 to U-3 accumulated during sea level fall to lowstand conditions, when sediment supply from the Mississippi River was rapidly increasing due the basinward progradation of the Mississippi Delta (Niedoroda et al., 2003a, Pirmez et al., 2012, Fig. 21g). During this interval, sea surface freshening caused by the strengthened Mississippi discharge reduced the intensity of Loop Current and consequently its impact on the sea floor (Nürnberg et al., 2008). Energetic bottom currents impacted the study area during the deposition of unit U-1 (and possibly the first part of Unit U-2), as testified by the presence of large furrow fields on horizon H1 (Fig. 8). If compared with the modern sea floor, the furrows on horizon H1 present a similar direction but deeper and larger scours, probably reflecting higher flow velocity (Flood, 1983) and consequently an increased ocean bottom circulation. The identification of palaeocurrent indicators derived from palaeo-sea floor surfaces and sediment thickness distributions highlights that the Loop Current, and related bottom currents (Hamilton, 2009), have existed during the entire time interval investigated in this study, which probably spans the last glacial-interglacial cycle, and that more energetic bottom currents characterize sea level highstands.

6.2. Nature, timing and triggers of MTCs

The role of bottom currents as a potential trigger of sea floor instabilities has been explored in different slope settings where large contourite drifts tend to develop (Laberg and Camerlenghi, 2008; Elliott et., 2010; Rashid et al., 2017). In salt-dominated slopes, however, disentangling the role of bottom currents and salt-driven tectonics in promoting the formation of submarine landslides is still poorly investigated (Prieto et al., 2016), as it is often difficult to reconstruct the provenance, timing and nature of MTCs generated by different processes. In the present study, 3D-HR seismic data coupled with chronological information allowed the identification of three different types of mass transport complexes and the discussion of their mechanism of emplacement in a sequence-stratigraphic framework (Fig. 22). Type 1 MTCs, bounded by horizons H3 and H5 at the base and at the top, respectively (Figs. 10, 12), formed between ca. 75 kyr and 25 kyr BP (Fig. 21), during a period of sea level lowering and increasing sediment supply to the basin (Kolla and Perlmutter, 1993; Slowey et al., 2003; Pirmez et al., 2012; Figs. 21g, 22). The formation of Type 1 MTCs is probably genetically linked to the growth of the mounded sediment ridge: as observed in other margin settings, sediment drifts and contourites tend to develop instability phenomena when a reduction of the sediment critical shear stress is generated by a combination of steep depositional slopes, relatively high sedimentation rates, good sediment sorting and high pore water content (Laberg and Camerlenghi, 2008; Rashid et al., 2017). Type 2 MTCs associated with sediment depocenter SD-5 formed between ca. 25 and 15 kyr BP, during the MIS 2 sea level lowstand (Figs. 21b, g, 22). At that time, the sediment accumulation rates in the Gulf of Mexico (Fig. 21g), and indeed in the study area (core CSS-1 in Figure 21g, Slowey et al., 2003), were at maximum. The emplacement of this type of MTC implies an energetic process, as testified by the presence of deep scours and grooves at the base of the landslide and by the large run-out distance (Table 1). A second Type 2 mass failure deposit is associated with the large erosional surface of horizon H0 (Fig. 7). Based on the chronological constraints available, the emplacement of this mass failure event can be

dated back to the MIS 6 (Fig. 21f), a period characterized by lower sea level and increased sediment supply to the basin (Figs. 21b, g).

During glacial intervals, salt-tectonic activity and the movement of the salt sheet basinward were promoted by a combination of sea level fall and rapid loading of the TX-LA Slope, the latter generated through the sediment supply from the Mississippi River (Humphris, 1979). Although the rate of salt deformation could be variable along the Sigsbee Escarpment, with also a potential delay time between the maximum salt movement and the application of the load (Roberts and Carney, 1997), halokinesis may have favoured the oversteepening of the Sigsbee Escarpment triggering the large type 2 mass failure events. MTCs formed under similar environmental conditions and at approximately the same age have been observed along the Sigsbee Escarpment outside the study area (Orange et al., 2003a; Young et al., 2003) as well as in salt withdrawal intraslope minibasins (Madof et al., 2009; Tripsanas et al., 2004; Salazar et al., 2014). Type 3 MTCs accumulated at the base of the Sigsbee Escarpment, remaining confined in the troughs of the sediment drifts (Figs. 18, 19). Type 3 MTCs identified in this study are described in the literature as debris flow deposits which were generated along the lower portion of the escarpment at the beginning of the Holocene during the post-glacial sea level rise (Niedoroda et al., 2003a; Orange et al., 2003a).). At that time sedimentation rate reduced from up to 7 mm/yr to ca. 0.12 mm/yr (core CSS-1 in Figure 21g, Slowey et al., 2003). This drastic change has been interpreted to reflect the effect of sea level fluctuations in controlling the loci and rates of sediment delivery to the deep water environment (Slowey et al., 2003). While during the first part of the deglaciation the water generated by the melting of the North American Ice Sheets drained along the Mississippi River directly into the Gulf of Mexico, at ca. 13 kyr BP the drainage system was partially captured by the Saint Lawrence Seaway, then feeding directly into the Atlantic Ocean (Broecker et al., 1989) and further reducing sediment supply to the Gulf of Mexico. Type 3 MTCs were probably generated by the failure of soft sediment pockets accumulating on the steep faces of the Sigsbee Escarpment, as suggested by Niedoroda et al. (2003a). These debris flow deposits promoted armouring of the sea floor protecting

the underlying sediment from erosion and reworking by bottom currents (Fig. 19). Mass failures reduced in size and frequency during the post-glacial sea level rise, with the last event occurring at ca. 3000 yr BP (Young et al., 2003), suggesting a strong correlation between salt movement, sea level change and sediment supply (Orange et al., 2003a).

7. Conclusion

The analysis of current-driven depositional features imaged through 3D-HR seismic data and multibeam bathymetry from the Sigsbee Escarpment suggests oscillations in the strength of the deep water Gulf of Mexico circulation during the last glacial-interglacial cycles. Fast bottom currents characterize sea level highstands, as testified by the presence of extensive furrow fields in both the modern sea floor and MIS 5e palaeo-sea floor horizon, while reduced bottom activity occurs during sea level lowstands. This alternation probably reflects the impact of the Mississippi River fresh water discharge (highest during sea level lowstands) on the Loop Current, which is considered the main driver on the deep water ocean circulation. The recognition of three types of mass transport complexes, each characterized by specific morphology, facies architecture, timing of deposition, location of the head scarp and trigger mechanisms, allowed the investigation of the role of sediment supply, halokinesis and bottom current activity in generating sea floor instability along the Sigsbee Escarpment. Type 1 MTCs, genetically linked to the growth of deep water sediment drifts, formed during sea level fall conditions when sediment accumulation in the Gulf of Mexico was rapidly increasing. Type 1 MTCs are characterized by short run-out distances, roughly planar basal surface, the presence of landslide blocks, and head scarps located in the upper continental rise. The emplacement of type 2 MTCs occurred during sea level lowstands: at that time fast sediment loading triggered halokinesis and the oversteepening of the Sigsbee Escarpment, generating the collapse of large portion of the slope. Type 2 MTCs show an energetic mechanism of emplacement with large volumes of sediment involved, long run-out distances and deep basal erosion. Type 3 MTCs formed during sea level rise to highstand conditions and mostly consist of debris flow

deposits which originated along the lower slope of the Sigsbee Escarpment. The recognition of different types of MTCs promotes not only a deeper understanding of the main drivers of margin instability along the Sigsbee Escarpment during the last glacial-interglacial cycle, but also may be of help in developing future hazard scenarios.

The complex interplay between the formation of MTCs and the accumulation of sediment by bottom currents is evident in this system. Instability of large sediment drifts resulted in locally-generated type 1 MTCs. Conversely, the topography resulting from the presence of MTCs of both types 1 and 2, and also of the sediment drifts, had an ongoing influence on the loci of sediment deposition by bottom currents. It is clear that the topography generated by these processes has persisted albeit with continuous modifications, over more than 100 kyr and through ca. 100 metres of stratigraphy.

We can conclude that sea-floor topography is the result of multiple processes that continuously modify inherited features, whose origin may be due to processes and conditions entirely different from any that are active on the sea floor today.

Acknowledgments

We are grateful to BP for the provision of both sea-floor and subsurface data. We thank the journal editor Michele Rebesco for his continuous support, and Lorena Moscardelli, Daniele Casalbore and an anonymous reviewer for their detailed and constructive comments, which have allowed us to considerably improve the manuscript.

8. References

Al-Khafaji, Z.A., Young, A.G., DeGroff, W., Humphrey, G.D., 2003. Geotechnical properties of the Sigsbee Escarpment from deep soil borings. Proceedings, OTC-15158-MS, Offshore Technology Conference, Houston, Texas.

Alves, T.M., Cartwright, J.A., 2010. The effect of mass-transport deposits on the younger slope morphology, offshore Brazil. Marine and Petroleum Geology 27, 20-27-2036.

Alves, T.M., Kurtev, K., Moore, G.F., Stresser, M., 2014. Assessing the internal character, reservoir potential, and seal competence of mass-transport deposits using seismic texture: A geophysical and petrophysical approach. AAPG Bulletin 98, 793-824.

Bianchi, G.G., McCave, I.N., 1999. Holocene periodicity in North Atlantic climate and deep-ocean flow south of Iceland. Nature 379, 515-517.

Blum, M., Pecha, M., 2014. Mid-Cretaceous to Paleocene North American drainage reorganization from detrital zircons. Geology 42, 607-610.

Broecker, W., Kennett, J., Flower, B., Teller, J., Trumbore, S., Bonani, G., Wolfli, W., 1989. Routing of meltwater from the Laurentide Ice-Sheet during the Younger Dryas Cold Episode. Nature 341, 318-321.

Brown, A.R., 2011. Interpretation of Three-Dimensional Seismic Data, 7th Edition. AAPG Memoir 42. Society of Exploration Geophysicists and American Association of Petroleum Geologists, pp. 665, Tulsa, Oklahoma.

Bryn, P., Berg, K., Forsberg, C.F., Solheim, A., Kvalstad, T.J., 2005a. Explaining Storegga Slide. Marine and Petroleum Geology 22, 11-19.

Bryn, P., Berg, K., Stoker, M.S., Haflidason, H., Solheim, A., 2005b. Contourites and their relevance for mass wasting along the Mid-Norwegian Margin. Marine and Petroleum Geology 22, 85-96.

Buffler, R.T., 1983. Structure of the Sigsbee Scarp, Gulf of Mexico. In: Bally, A.W., (eds.), Seismic Expression of Structural Styles- A Picture and Work Atlas. AAPG Studies in Geology 15(2):2.3-2.5.

Campbell, D.C., Deptuck, M., 2012. Alternating bottom-current-dominated and gravity-flow-dominated deposition in a lower slope and rise setting – Insights from the seismic geomorphology of the Western Scotian Margin, Eastern Canada. In: Application of the Principles of Seismic Geomorphology to Continental-Slope and Base-of-Slope Systems: Case Studies from Seafloor and Near-Seafloor Analogues. SEPM Special Publication 99, 329-346.

Canals, M., Puig, P., Durrieu de Madron, X., Heussner, S., Palanques, A., Fabres, J., 2006. Flushing submarine canyons. Nature 444, 354-357.

Casalbore, D., Bosman, A., Chiocci, F.L., 2012. Study of recent small-scale landslides in geologically active marine areas through repeated multibeam surveys: examples from the southern Italy. In: Yamada, Y., Kawamura, K., Ikehara, K., Ogawa, Y., Urgeles, R., Mosher, D., Chaytor, J., Strasser, M. (Eds.), Submarine Mass Movements and Their Consequences: Advances in Natural and Technological Hazards Research, Springer Netherlands, Kiel, Germany, pp. 573-582

Cattaneo, A., Correggiari, A., Langone, L., Trincardi, F., 2003. The late-Holocene Gargano subaqueous delta Adriatic shelf: sediment pathways and supply fluctuations. Marine Geology 193, 61-91.

Chiocci, F.L., Casalbore, D., 2017. Unexpected fastrate of morphological evolution of geologically-active continental margins during the Quaternary: Examples from selected areas in the Italian seas. Marine and Petroleum Geology 82, 154-162.

Chen, Q., Sidney, S., 1997. Seismic attribute technology for reservoir forecasting and monitoring. The Leading Edge 16, 445-448.

Coleman, J.M., Roberts, H.H., Bryant, W.R., 1986. Late Quaternary sedimentation. In: Salvador, A., The Gulf of Mexico Basin. Geological Society of America, The geology of North America, v. J, pp. 325-352.

Cooper, C., Forristall, G.Z., Joyce, T.M., 1990. Velocity and hydrographic structure of two Gulf of Mexico warm-core rings. Journal of Geophysical Research 95, 1663-1679.

Diegel, F.A., Karlo, J.F., Schuster, D.C., Shoup, R.C., Tauvers, P.R., 1995, Cenozoic structural evolution and tectonostratigraphic framework of the northern Gulf Coast continental margin. In: Jackson, M.P.A., Roberts, D.G., Snelson, S. (Eds.), Salt Tectonics: A Global Perspective. American Association of Petroleum Geologists Memoir 65, pp. 153-175

Dillon, W.P., Danforth, W.W., Hutchinson, D.R., Drury, R.M., Taylor, M.H., Booth, J.S., 1998. Evidence for faulting related to dissociation of gas hydrate and release of methane off the southeastern United States. In: Henriet, J.-P., Mienert, J. (Eds.), Gas Hydrates: Relevance to world margin stability and climate change, Geological Society of London Special Publication 137, 275-291.

Dunlap, D.B., Wood, L.J., Moscardelli, L.G., 2013. Seismic geomorphology of early North Atlantic sediment waves offshore northwest Africa. Interpretation 1, 75-91.

Elliott, G.M., Shannon, P.M., Haughton, P.D.W., Øvrebø, L.K., 2010. The Rockall Bank Mass Flow: Collapse of a moated contourite drift onlapping the eastern flank of Rockall Bank, west of Ireland. Marine and Petroleum Geology 27, 92-107.

Faugères, J-C., Stow, D.A.V., Imbert, P., Viana, A., 1999. Seismic features diagnostic of contourite drifts. Marine Geology 162, 1-38.

Fildani, A., McKay, M.P., Stockli, D., Clark, J., Dykstra, M.L., Stockli, L., Hessler, A.M., 2017. The ancestral Mississippi drainage archived in the late Wisconsin Mississippi deep-sea fan. Geology 44, 479-482.

Flood, R.D., 1983. Classification of sedimentary furrows and a model for furrow initiation and evolution. Geological Society of America Bulletin 94, 630-639.

Gee, M.J.R., Gawthorpe, R.L., Friedmann, J.S., 2005. Giant striations at the base of a submarine landslide. Marine Geology 214, 287-294.

Gong, C., Steel, R.J., Wang, Y., Lin, C., Olariu, C., 2016. Shelf-margin architecture variability and its role in sediment-budget partitioning into deep-water areas. Earth-Science Reviews 154, 72-101.

Grant, K.M., Rohling, E.J., Bronk Ramsey, C., Cheng, H., Edwards, R.L., Florindo, F., Heslop, D., Marra, F., Roberts, A.P., Tamisiea, M.E., Williams, F., 2014. Sea-level variability over five glacial cycles. Nature Communications 5.5076.

Hamilton, P., 1990. Deep currents in the Gulf of Mexico. Journal of Physical Oceanography 20, 1087-1104.

Hamilton, P., 2009. Topographic Rossby waves in the Gulf of Mexico. Progress in Oceanography 82, 1-31.

Hampton, M.A., Lee, H.J., Locat, J., 1996. Submarine landslides. Reviews of Geophysics 34, 33-59.

Harders, R., Ranero, C.R., Weinrebe, W., Behrmann, J.H., 2011. Submarine slope failures along convergent continental margin of the Middle America Trench. Geochemistry, Geophysics, Geosystems 12, Q05S32, doi:10.1029/2010GC003401.

Heezen, B.C., Ewing, M., 1952. Turbidity currents and submarine slumps and the 1929 Grand Banks earthquake. Am. J. Sci. 250, 849-873.

Henkel, D.J., 1970. The role of waves in causing submarine landslides. Géotechnique 20, 75-80.

Hernández-Molina, F.J., Larter, R.D., Rebesco, M., Maldonado, A., 2006. Miocene reversal of bottom water flow along the Pacific Margin of the Antarctic Peninsula: Stratigraphic evidence from a contourite sedimentary tail. Marine Geology 228, 93-116.

Hernández-Molina, F.J., Llave, E., Stow, D.A.V., 2008a. Abyssal plain contourites. In: Rebesco, M., Camerlenghi, A. (Eds.), Developments in Sedimentology. Elsevier, Amsterdam, 347-378.

Hernández-Molina, F.J., Maldonado A., Stow, D.A.V., 2008b Continental slope contourites. In: Rebesco, M., Camerlenghi, A. (Eds.), Developments in Sedimentology. Elsevier, Amsterdam, 379-408.

Huh, O.K., Wiseman, W.J., Rouse, L.J., 1981. Intrusion of Loop Current waters onto the west Florida continental shelf. Journal of Geophysical Research 86, 4186-4192.

Humphris, C.C.Jr., 1979. Salt Movement on Continental Slope, Northern Gulf of Mexico. AAPG Bulletin 63, 782-798.

Kennett, J.P., Cannariato, K.G., Hendy, I.L., Behl, R.J., 2000. Carbon isotopic evidence for methane hydrates instability during Quaternary interstadials. Science 288, 128-133.

Kennett, J., Cannariato, K.G., Hendy, I.L., Behl, R.J., 2003. Methane hydrates in Quaternary climate change: The clathrate gun hypothesis: Washington, D.C. American Geophysical Union, 216 p.

Kneller, B., 1995. Beyond the turbidite paradigm: physical models for deposition of turbidites and their implications for reservoir prediction. Geological Society, London, Special Publications 94, 31-49.

Kneller, B., Dykstra, M., Fairweather, L., Milana, JP., 2016. Mass-transport and slope accommodation: Implications for turbidite sandstone reservoirs. AAPG Bulletin 100, 213-235.

Kolla, V., Perlmutter, M.A., 1993. Timing of turbidite sedimentation on the Mississippi Fan. AAPG Bulletin 77, 1129-1141.

Kvenvolden, K.A., 1999. Potential effects of gas hydrates on human welfare. PNAS 97, 3420-3426.

Laberg, J.S., Camerlenghi, A., 2008. The significance of contourites for submarine slope stability. In: Rebesco, M., Camerlenghi, A. (Eds.), Developments in Sedimentology 60, 537-556. Elsevier, Amsterdam.

Laberg, J.S., Baeten, N.J.,Vanneste, M., Forsberg, C.F., Forwick, M., Haflidason, H., 2016. Sediment failure affecting muddy contourites on the continental slope offshore Northern

Norway: lessons learned and some outstanding issues. In: Submarine Mass Movements and their Consequences. Springer, pp. 281-289.

Lee, Y.D., George, R.A., 2004. High-resolution geological AUV survey results across a portion of the eastern Sigsbee Escarpment. AAPG Bull. 88, 747-764.

Li, W., Alves, T.M., Wu, S., Rebesco, M., Zhao, F., Mi, L., Ma, B., 2016. A giant, submarine creep zone as a precursor of large-scale slope instability offshore the Dongsha Islands (South China Sea). Earth and Planetary Science Letters 451, 272-284.

Liu, X., Flemings, P., 2009. Dynamic response of oceanic hydrates to sea level drop. Geophysical Research Letters 36, L17308, doi:10.1029/2009GL039821.

Locat, J., Lee, H.J., 2005. Subaqueous debris flows. In: Jakob, M., Hungr, O. (Eds.), Debris-flows hazards and related phenomena. Springer, Berlin.

Madof, A.S., Christie-Blick, N., Anders, M.H., 2009. Stratigraphic controls on a salt-withdrawal intraslope minibasin, north-central Green Canyon, Gulf of Mexico: Implications for misinterpreting sea level change. AAPG Bulletin 83, 535-561.

Martin, R.G., 1978. Northern and eastern Gulf of Mexico continental margin: Stratigraphic and structural framework, pp. 21-42. In: A.H. Bouma, G.T. Moore, and J.M. Coleman (Eds.), Framework, Facies, and Oil-trapping Characteristics of the Upper Continental Margin. AAPG Studies in Geology 7.

Martin, R.G., Bouma, A.H., 1978. Physiography of Gulf of Mexico, pp. 3-19. In: Bouma, G.T.M., Coleman, J.M. (Eds.), Framework, Facies, and Oil Trapping Characteristics of the Upper Continental Margin. AAPG Studies in Geology 7.

Martorelli, E., Bosman, A., Casalbore, D., Falcini, F., 2016. Interaction of downslope and along-slope processes off Capo Vaticano (southern Tyrrhenian Sea, Italy), with particular reference to contourite-related landslides. Marine Geology 378, 43-55.

Maslin, M., Owen, M., Day, S., Long, D., 2004. Linking continental-slope failures and climate change: Testing the clathrate gun hypothesis. Geology 32, 53-56.

Masson, D.G., Howe, J.A., Stoker, M.S., 2002. Bottom-current sediment waves, sediment drifts and contourites in the northern Rockall Trough. Marine Geology 192, 215-237.

Masson, D.G., Wynn, R.B., Bett, B.J., 2004. Sedimentary environment of the Faroe-Shetland and Faroe Bank Channels, north-east Atlantic, and the use of bedforms as indicators of bottom current velocity in the deep ocean. Sedimentology 51, 1207-1241.

Masson, D.G., Harbitz, C.B., Wynn, R.B., Pedersen, G., Løvholt F., 2006. Submarine landslides: processes, triggers and hazard prediction. Philosophical Transactions of the Royal Society A 364, 2009-2039.

McAdoo, B.G., Pratson, L.F., Orange, D.L., 2000. Submarine landslide geomorphology, US continental slope. Marine Geology 169, 103-136.

McCave, I.N., Manighetti, B., Robinson, S.G., 1995. Sortable silt and fine sediment size/composition slicing: Parameters for paleocurrent speed and palaeoceanography. Paleoceanography 10, 593-610.

Mienert, J., Posewang, J., Baumann, M., 1998. Gas hydrates along the north-eastern Atlantic margin: Possible hydrate-bound margin instabilities and possible release of methane. In: Henriet, J.-P., Mienert, J. (Eds.), Gas Hydrates: Relevance to world margin stability and climate change, Geological Society of London Special Publication 137, 275-291.

Miramontes, E., Cattaneo, A., Jouet, G., Thereau, E., Thomas, Y. Rovere, M., Trincardi, F., 2016. The pianosa contourite depositional system (northern Tyrrhenian sea): drift morphology and plio-quaternary stratigraphic evolution. Marine Geology 378, 20-42.

Miramontes, E., Garziglia, S., Sultan, S., Jouet, G., Cattaneo, A., 2018. Morphological control of slope instability in contourites: a geotechnical approach. Landslides https://doi.org/10.1007/s10346-018-0956-6.

Moore, G.T., Starke, G.W., Bonham, L.C., Woodbury, H.O., 1978. Mississippi Fan, Gulf of Mexico-physiography, stratigraphy, and sedimentational patterns. AAPG Bulletin 62, 155-191.

Moscardelli, L., Wood, L., Mann, P., 2006. Mass-transport complexes and associated processes in the offshore area of Trinidad and Venezuela. AAPG Bulletin 90, 1059-1088.

Moscardelli, L., Wood, L., 2008. New classification system for mass transport complexes in offshore Trinidad. Basin Research 20, 73-98.

Mulder, T., Syvitski, J.P.M., 1995. Turbidity currents generated at river mouths during exceptional discharges to the world oceans. The Journal of Geology 103, 285-299.

Mulder, T., Cochonat, P., 1996. Classification of offshore mass movements. Journal of Sedimentary Research 66,43-57.

Mutti, E., Normark, W.R., 1991. An integrated approach to the study of turbidite systems. In: Weimer. P., Link, H. (Eds.), Seismic facies and sedimentary processes of submarine fans and turbidite systems, Springer, New York, p. 75-106.

Nadim, F., Krunic, D., Jeanjean, P., 2003. Deterministic slope stability analyses of the Sigsbee Escarpment. Proceedings, OTC-15203-MS, Offshore Technology Conference, Houston, Texas.

Nibbelink, K., 1999. Modeling deepwater reservoir analogs through analysis of recent sediments using coherence, seismic amplitude, and bathymetry data, Sigsbee escarpment, Green Canyon, Gulf of Mexico. The Leading Edge 18, 550-561.

Niedoroda, A.W., Jeanjean, P., Driver, D., Reed, C., Hatchett, L., Briaud, J.-L., Bryant, W., 2003a. Bottom Currents, Deep Sea Furrows, Erosion Rates, and Dating Slope Failure-Induced Debris Flows Along the Sigsbee Escarpment in the Deep Gulf of Mexico. Proceedings, OTC-15199-MS, Offshore Technology Conference, Houston, Texas.

Niedoroda, A.W., Reed, C.W., Hatchett, L., Young, A., Lanier, D., Kasch, V., Jeanjean, P., Orange, D.L., Bryant, W., 2003b. Analysis of past and future debris flows and turbidity currents generated by slope failures along the Sigsbee Escarpment in the deep Gulf of Mexico. Proceedings, OTC-1162-MS, Offshore Technology Conference, Houston, Texas.

Nisbet, E., Piper, D.W., 1998. Giant submarine slides. Nature 392, 329-330.

Nowacki, F., Solhejell, E., Nadim, F., Liedtke, E., Andersen, K.H., Andresen, L., 2003. Deterministic slope stability analyses of the Sigsbee Escarpment. Proceedings, OTC-15160-MS, Offshore Technology Conference, Houston, Texas.

Nowlin, W.D., 1972. Winter Circulation Patterns and Property Distributions, pp. 3-51. In: Capurro, L.R.A., Reid, J.L. (Eds.), Contributions on the Physical Oceanography of the Gulf of Mexico. Gulf Publishing Co.

Nowlin, W.D., Jochens, A.E., Reid, R.O., Di Marco, S.F., 1998. Texas-Louisiana Shelf Circulation and Transport Processes Study: Synthesis Report, Volume I: Technical Report. OCS Study MIMS 98-0035, U.S. Department of the Interior, Minerals Management Service, Gulf of Mexico OCS Region. 502 pp.

Nürnberg, D., Ziegler, M., Karas, C., Tiedemann, R., Schmidt, M.W., 2008. Interacting Loop Current variability and Mississippi River discharge over the past 400 kyr. Earth and Planetary Science Letters 272, 278-289.

Orange, D.L., Angell, M., Brand, J., Thomson, J., Buddin, T., Williams, M., Hart, W., Berger III, W., 2003a. Geological and Shallow Salt Tectonic Setting of the Mad Dog and Atlantis Fields: Relationship between Salt, Faults, and Seafloor Geomorphology. Proceedings, OTC-15157-MS, Offshore Technology Conference, Houston, Texas.

Orange, D.L., Saffer, D., Jeanjean, P., Al-Khafaji, Z., Riley, G., Humphrey, G., 2003. Measurements and modeling of the shallow pore pressure regime at the Sigsbee Escarpment: Successful prediction of overpressure and ground-truthing with borehole measurements. Proceedings, OTC-15201-MS, Offshore Technology Conference, Houston, Texas.

Peel, F.J., Travis, C.J., Hossack, J.R., 1995. Genetic structural provinces and salt tectonics of the Cenozoic offshore U.S. Gulf of Mexico: A preliminary analysis. I: Jackson, M.P.A., Roberts, D.G., Snelson, S. (Eds.), Salt Tectonics: A Global Perspective. American Association of Petroleum Geologists Memoir 65, pp. 153-175.

Pellegrini, C., Maselli, V., Trincardi, F., 2016. Pliocene-Quaternary contourite depositional system along the south-western Adriatic margin: changes in sedimentary stacking pattern and associated bottom currents. Geo-Marine Letters 36, 67-79.

Pellegrini, C., Maselli, V., Gamberi, F., Asioli, A., Bohacs, K.M., Drexler, T.M., Trincardi, F., 2017. How to make a 350-m-thick lowstand systems tract in 17,000 years: The Late Pleistocene Po River (Italy) lowstand wedge. Geology 45, 327-330.

Pirmez, C., Prather, B.E., Mallarino, G., O'Hayer, W.W., Droxler, A.W., Winker, C.D., 2012. Chronostratigraphy of the Brazos-Trinity depositional system, western Gulf of Mexico: implications for deepwater depositional models. In: Prather, B.E., Deptuck, M.E., Mohrig, D., Van Hoorn, B., Wynn, R.B. (Eds.), Application of the Principles of Seismic Geomorphology to Continental-Slope and Base-of-slope Systems: Case Studies from Seafloor and Near-seafloor Analogues, SEPM Special Publication 99, 111-143, Tulsa, Oklahoma.

Poore, R.Z., Dowsett, H.J., Verardo, S., Quinn, T.M., 2003. Millennial- to century-scale variability in Gulf of Mexico Holocene climate records. Paleoceanography 18, doi:10.1029/2002PA000868.

Porębski, S.J., Steel, R.J., 2003. Shelf-margin deltas: their stratigraphic significance and relation to deepwater sands. Earth-Science Reviews 62, 283-326.

Prieto, M.I., Moscardelli, L., Wood, L.J., 2014. Investigating modern ultra deepwater sedimentary processes in the central Gulf of Mexico using high resolution geophysical data. Proceedings, OTC-2510-MS, Offshore Technology Conference, Houston, Texas.

Prieto, M.I., 2016. Sediment gravity-driven vs. bottom-current-controlled processes and interactions: A study of multiple geomorphic domains in the central Gulf of Mexico and comparison with global systems. PhD dissertation. The University of Texas at Austin.

Prieto, M.I., Moscardelli, L., Wood, L.J., 2016. Exploring the influence of deepwater currents as potential triggers for slope instability. Submarine Mass Movements and their Consequences 41, 331-338.

Puig, P., Palanques, A., Orange, D.L., Lastras, G., Canals, M., 2008. Dense shelf water cascades and sedimentary furrow formation in the Cap de Creus Canyon, northwestern Mediterranean Sea. Continental Shelf Research 28, 2017-2030.

Rashid, H., MacKllop, K., Sherwin, J., Piper, D.J.W., Marche, B., Vermooten, M., 2017. Slope instability on a shallow contourite-dominated continental margin, southeastern Grand Banks, eastern Canada. Marine Geology 393, 203-215.

Rebesco, M., Hernández-Molina, F.J., Van Rooij, D., Wåhlind, A. 2014. Contourites and associated sediments controlled by deep-water circulation processes: State-of-the-art and future considerations. Marine Geology 352, 111-154.

Rijks, E.J.H., Jauffred, J.C.E.M., 1991. Attribute extraction: An important application in any detailed 3-D interpretation study. The Leading Edge 10, 11-19.

Roberts, H.H., Carney, R.S., 1997. Evidence of episodic fluid, gas and sediment venting on the Northern Gulf of Mexico continental slope. Economic Geology 92, 863-879.

Salazar, J.A., Knapp, J.H., Knapp, C.C., Pyles, D.R., 2014. Salt tectonics and Pliocene stratigraphic framework at MC-118, Gulf of Mexico: An integrated approach with application to deep-water confined structures in salt basins. Marine and Petroleum Geology 50, 51-67.

Shanmugam, G., 2006. Deep-Water Processes and Facies Models: Implications for Sandstone Petroleum Reservoirs, Volume 5, 1st Edition, pp. 496, Elsevier Science.

Slowey, N. C., Bryant, W. R., Bean, D. A., Young, A. G., Gartner, S., 2003. Sedimentation in the vicinity of the Sigsbee Escarpment During the Last 25,000 Years. Proceedings, OTC 15159, Offshore Technology Conference, Houston, Texas.

Stow, D.A.V., Hernández-Molina, F.J., Llave, E., Sayago-Gil. M., Díaz del Río, D., Branson, A., 2008. Bedform-velocity matrix: The estimation of bottom current velocity from bedform observations. Geology 45, 327-330.

Sturges, W., 1993. The annual cycle of the western boundary current in the Gulf of Mexico. Journal of Geophysical Research 98, 18053-18068.

Suter, J.R., Berryhill, Jr. H.L., 1985. Late Quaternary shelf-margin deltas, Northwest Gulf of Mexico. AAPG Bulletin 69, 77-91.

Swierz, A. M., 1992. Seismic stratigraphy and salt tectonics along the Sigsbee Escarpment, southeastern Green Canyon region. In: Geyer, R.A. (Eds.), CRC Handbook of Geophysical Exploration at Sea, 2nd Edition, CRC Press, Inc., Boca Raton, Florida, pp. 227-294.

Tappin, D.R., Grilli, S.T., Harris, J.C., Geller, R.J., Masterlak, T., Kirby, J.T., Shi, F., Ma, G., Thingbaijam, K.K.S., Mai, P.M., 2014. Did a submarine landslide contribute to the 2011 Tohoku tsunami? Marine Geology 357, 344-361.

Talling, P.J., Wynn, R.B., Masson, D.G., Frenz, M., Cronin, B.T., Schiebel, R., Akhmetzhanov, A.M., Dallmeier-Tiessen, S., Benetti, S., Weaver, P.P.E., Georgiopoulou, A., Zühlsdorff, C., Amy, L.A., 2007. Onset of submarine debris flow deposition far from original giant landslide. Nature 450, 541-544.

Trincardi, F., Verdicchio, G., Miserocchi, S., 2007. Seafloor evidence for the interaction between cascading and along-slope bottom water masses. Journal of Geophysical Research 112, F03011, doi:10.1029/2006JF00062.

Tripsanas, E.K., Bryant, W.R., Phaneuf, B.A., 2004. Slope-instability processes caused by salt movements in a complex deep-water environment, Bryant Canyon area, northwest Gulf of Mexico. AAPG Bulletin 88, 801-823.

von Huene, R., Pecher, I., 1999. Vertical tectonics and the origins of BSRs along the Peru margin. Earth Planet. Sci. Letters 166, 47-55.

Wolinsky, M.A., Pratson, L.F., 2007. Overpressure and slope stability in prograding clinoforms: Implications for marine morphodynamics. Journal of Geophysical Research 112, F04011, Doi:10.1029/2007JF000770.

Young, A., Bryant, W., Slowey, N., Brand, J., Gartner, S., 2003. Age Dating of Past Slope Failures of the Sigsbee Escarpment within Atlantis and Mad Dog Developments. Proceedings, Offshore Technology Conference, Houston, Texas.

Zang, M., Huang, Y., Bao. Y., 2016. The mechanism of shallow submarine landslide triggered by storm surge. Natural hazards 81, 1373-1383.

Ziegler, M., Nürnberg, D., Karas, C., Tiedemann, R., Lourens, L.J., 2008. Persistent summer expansion of the Atlantic Warm Pool during glacial abrupt cold events. Nature Geoscience 1, 601-605.

Figure Captions

Figure 1- Digital elevation model of the Gulf of Mexico basin and surrounding lands with main geomorphic elements. Yellow arrows: surficial ocean circulation; light blue arrow: direction of deep water currents along the Sigsbee Escarpment (from Hamilton, 2009); red square: study area; stars: location of the sediment cores presented in Figure 21. DEM data from GEBCO.

Figure 2- 3D view of the study area with main structural and depositional elements. MTC: Mass Transport Complex; Sd: Sediment drift.

Figure 3- Shaded relief map of the sea floor above the Atlantis field. Green square: 3D seismic data coverage; red area: extent of the seismic attribute maps; yellow lines (numbered from 1 to 9): arbitrary lines extracted from the seismic volume and presented in this study; orange dots (ASB-3 and ASB-4): location of soil boreholes; white square: extent of the AUV multibeam bathymetric map presented in Figure 19. The black arrows indicate multibeam acquisition artefacts, which are visible as NW-SE oriented discontinuities.

Figure 4- Seismic lines 1 and 2 (see location in Figure 3) showing the eight seismic horizons investigated in this study (H0 to H7).

Figure 5- Close-up views of the seismic facies characterizing each horizon and unit described in the text.

Figure 6- Seismic lines 3 and 4 (see location in Figure 3) showing the eight seismic horizons investigated in this study (H0 to H7).

Figure 7- a: Surface elevation map of horizon H0 with 50 m spacing contours; note the N-S trending ridge. b: RMS amplitude map of H0; note the seismic acquisition artefacts represented by NW-SE oriented lineaments of low RMS values (black arrows). c: Variance map of H0. d: Thickness map of unit U-1 with sediment depocenter SD-1. e (left): Simplified bathymetry (50 m spacing contours) with the ridge (black dashed line), topographic depressions α and β, scalloped margin (black line), and locations of cross sections AB and CD (red lines). e (right): cross sections AB and CD on horizons H0 (red line) and H1 (grey line).

Figure 8- a: Surface elevation map of horizon H1 with 50 m spacing contours; note the N-S trending ridge. b: RMS amplitude map of H1; note the area characterized by high RMS amplitude values (red dashed lines). c: Variance map of H1; note the furrows fields. d: Thickness map of unit U-2 with sediment depocenters SD-1 and SD-2. e (left): Simplified bathymetry (50 m spacing contours) with the ridge (black dashed line), the topographic depressions α and β, and locations of cross sections AB and CD (red lines). e (right): cross sections AB and CD on horizons H1 (red line) and H2 (grey line).

Figure 9- a: Surface elevation map of horizon H2 with 50 m spacing contours. The N-S trending ridge now shows a gentle topography due to the deposition of SD-1. b: RMS amplitude map of H2; note the area characterized by high RMS amplitude values (red dashed lines). c: Variance map of H2. d: Thickness map of Unit U-3 with sediment depocenters SD-1 and SD-2. e (left): Simplified bathymetry (50 m spacing contours) with topographic depressions α and β, and locations of cross sections AB and CD (red lines). e (right): cross sections AB and CD on horizons H2 (red line) and H3 (grey line).

Figure 10- a: Surface elevation map of horizon H3 with 50 m spacing contours; note the escarpment (see also Figure 11). b: RMS amplitude map of H3, with the spatial extent of SD-3 marked by the

black dashed line. The red dashed line in the NW corner confines the area characterized by high RMS amplitude values on the western side of the mounded ridge. c: Variance map of H3. d: Thickness map of Unit U-4 with sediment depocenter SD-3 (black dashed line). e (left): Simplified bathymetry (50 m spacing contours) with topographic depressions α and β, extent of SD-3 (light blue), cross sections AB and CD (red lines), and the position of seismic line 5 of Figure 11 (black line). e (right): cross sections AB and CD on horizons H3 (red line) and H4 (grey line). SD-3 fills the accommodation space available at the base of the escarpment (red arrow).

Figure 11- Seismic line 5 (see location in Figs. 3, 10). Sediment depocenter SD-3 (highlighted in light blue) is bounded by horizons H3 and H4. The head scarp, corresponding to the escarpment of Figure 10a, is marked by truncated reflections. Horizontal slices extracted at 10 metres intervals between -2470 metres and -2430 metres depth from the variance seismic cube (position marked by the black square on the seismic line) show the presence of sediment blocks. The seismic line also highlights the two sub-units (SD-4 lower and upper, divided by the yellow dashed line) which constitute sediment depocenter SD-4.

Figure 12- a: Surface elevation map of horizon H4 with 50 m spacing contours; note the escarpment. b: RMS amplitude map of H4; the black dashed lines represent the spatial extent of the sub-units SD-4 lower and upper, mapped on seismic profiles. The area with low RMS values (in light blue) located basinward of SD-4 lower corresponds to SD-3. c: Variance map of H4; note the high values associated with the escarpment and the sharp contact at the basinward limit of SD-4 lower. d: Thickness map of Unit U-5 with sediment depocenter SD-4; extent of sub-units SD-4 lower and upper marked by black dashed lines. e (left): Simplified bathymetry (50 m spacing contours) with topographic depressions α and β, sub-units SD-4 lower (light green) and SD-4 upper (orange), cross sections AB and CD (red lines) and the position of seismic line 6 of Figure 13 (black line). e (right): cross sections AB and CD on horizons H4 (red line) and H5 (grey line).

Figure 13- Seismic line 6 (see location in Figs. 3, 12). Sediment depocenter SD-3 (light blue) is bounded by horizons H3 and H4 while SD-4 is bounded by horizons H4 and H5. SD-4 is formed by two sub-units (SD-4 lower, in light green, and SD-4 upper, in orange) separated by a continuous and high-amplitude reflection marked by the yellow dashed line. The seismic line highlights the toe of the lower landslide (black arrow, visible also in Figs. 12b, c) at the transition from seismic facies 3 (characterized by transparent to chaotic reflections, in light green) to seismic facies 2 (showing parallel and continuous high amplitude reflections).

Figure 14- a: Surface elevation map of horizon H5 with 50 m spaced contours; note the two escarpments oriented WSW-ENE (red arrow). b: RMS amplitude map of H5 where the base of SD-5 is marked by the black dashed line. c: Variance map of H5; note the two escarpments oriented WSW-ENE (red arrow). d: Thickness map of Unit U-5 with the sediment depocenters SD-5 and SD-6 (red arrow). e (left): Simplified bathymetry (50 m spacing contours) with topographic depressions α and β, extent of SD-5 (red area bounded by black dashed lines), topographic cross sections AB and CD (red lines), and the position of seismic profiles 7 and 8 of Figure 15 (black lines). e (right): cross sections AB and CD on horizons H5 (red line) and H6 (grey line).

Figure 15- 3D view of the RMS amplitude derived from horizon H5 combined with seismic sections (lines 7 and 8, see location in Figs. 3, 14). While the sediment drift is characterized by low RMS values on a smooth topography, the base of landslide SD-5 (highlighted in red by horizon H5) shows higher values. The black dashed line marks the extent of the SD-5 as seen on seismic data. Seismic lines 7 and 8 highlight the basal grooves and the seismic facies of SD-5.

Figure 16- a: Surface elevation map of horizon H6 with 50 m spaced contours. b: RMS amplitude map of H6; the black dashed line marks the extent of SD-5. c: Variance map of H6. d: Thickness

map of Unit U-7 with sediment depocenter SD-7. e (left): Simplified bathymetry (50 m spacing contours) with topographic cross sections AB and CD (red lines). e (right): cross sections AB and CD on horizons H6 (red line) and H7 (grey line).

Figure 17- a: Surface elevation map of horizon H7 with 50 m spaced contours. b: RMS amplitude map of H7. c: Variance map of H7. d: Thickness map of Unit U-8 with sediment depocenters SD-7, SD-8 and SD-9. e (left): Simplified bathymetry (50 m spacing contours) with topographic cross sections AB and CD (red lines). e (right): cross sections AB and CD on horizons H7 (red line) and the sea floor (SF, grey line).

Figure 18- a: Surface elevation map of the sea floor extracted from the 3D-HR seismic cube with 50 m spaced contours; TL: topographic lows. b: RMS amplitude map of the sea floor horizon showing high RMS amplitude values (black dashed lines) where SD-8 and SD-9 accumulate. c: Variance map of the sea floor horizon highlights the presence of furrow fields impacting much of the study area. d: Simplified bathymetry (50 m spacing contours).

Figure 19- High-resolution slope map of the sea floor derived from AUV multibeam bathymetric data (see location in Figure 3) with 50 m spacing contours. TL: topographic lows.

Figure 20- Seismic tie to borehole ASB-4 (see location of the borehole and of seismic line 9 in Figure 3) with the chronology provided by Young et al. (2003). Only horizons H0 and H5 can be loop-tied with the borehole ASB-4 and ASB-3 (projected on the seismic line 9).

Figure 21- a: Marine Isotopic Stage (MIS). b: Relative Sea Level (RSL) curve, data from Grant et al. (2014). c: Age constraints from Young et al. (2003). d: Dated MTCs in the study area (Niedoroda et a., 2003a). e: Evidence of furrowed surfaces (the sea floor and horizon H1). f:

Proposed chronology of horizons H0 to H7. g: Sediment accumulation rates in the Gulf of Mexico basin from cores MD02-2575 (Ziegler et al., 2008), U1320 of IODP308 (Pirmez et al., 2012), CSS-1 (Slowey et al., 2003). Location of cores in Figure 1.

Figure 22- Conceptual model of the evolution of the study area based on the chronology of horizons H0 to H7 (Fig. 21). Relative Sea Level (RSL) curve, data from Grant et al. (2014).

Table 1. Morphometry and classification of mass transport complexes (MTCs) in the study area.

Table 1

	SD-3	SD-4 lower	SD4 upper	SD-5	SD-8	SD-9
Length (km)	8.9	8.3	>4.5	>16	3.3	2.8
Max thickness (m)	34	31	27	80	~6	~6
Area (km^2)	18	14	>13	>98	1.5	1
Volume (km^3)	0.43	0.52	0.4	>3	0.009	0.006
Source area	Deep water sediment drift			Sigsbee Escarpment	Lower slope of the Sigsbee Escarpment	
Type and Classification*	Type 1 (detached*) MTCs			Type 2 (attached*) MTCs	Type 3 (detached*) MTCs	

*definition from Moscardelli and Wood (2008)